Isomerization of Functionalized Olefins by Using the Dinuclear Catalyst $[Pd^{I}(\mu\text{-Br})(P^{t}Bu_3)]_2$: A Mechanistic Study

Special Issue

Debasis Koley,*[a] Sriman De,[a] Nardana Sivendran,[b] and Lukas J. Gooßen*[b]

Dedicated to Prof. Christian Bruneau on the occasion of his 70th birthday.

Abstract: In a combined experimental and computational study, the isomerization activity of the dinuclear palladium(I) complex $[Pd^{I}(\mu\text{-Br})(P^{t}Bu_3)]_2$ towards allyl arenes, esters, amides, ethers, and alcohols has been investigated. The calculated energy profiles for catalyst activation for two alternative dinuclear and mononuclear catalytic cycles, and for catalyst deactivation are in good agreement with the experimental results. Comparison of experimentally observed *E*/*Z* ratios at incomplete conversion with calculated kinetic selectivities revealed that a substantial amount of product must form *via* the *dinuclear pathway*, in which the isomerization is promoted cooperatively by two palladium centers. The dissociation barrier towards mononuclear Pd species is relatively high, and once the catalyst enters the energetically more favorable *mononuclear pathway*, only a low barrier has to be overcome towards irreversible deactivation.

Introduction

Catalytic double-bond migration within olefins and their functionalized analogs has tremendous importance in synthesizing industrially relevant chemicals.[1] Metal-catalyzed isomerization (Scheme 1)[2] is an efficient process with ideal atom economy, that is used in the synthesis of fine chemicals[3] and commodities,[4] and in the valorization of petroleum feedstocks.[5] The Takasago process is a prominent example which features the Ru/Tol-BINAP-catalyzed asymmetric isomerization of a prochiral enamine to produce menthol.[6]

The incorporation of isomerization steps in tandem catalysis has opened up further applications of isomerization catalysts (Scheme 2).[7] Examples of isomerizing functionalizations include isomerizing hydrocyanations, hydroformylations, or hydrocarboxylations,[5a,8] which allow generating valuable linear products from inexpensive internal olefins. In orthogonal tandem catalysis,[9] two different catalysts are independently yet cooperatively active within a single reaction vessel. Recent examples are isomerizing metatheses,[10] which involve the iterative, cooperative action of an isomerization and an olefin metathesis catalyst to convert single olefins or olefin mixtures into defined product blends with carbon-chain lengths evenly distributed around the mean chain length of the starting materials.

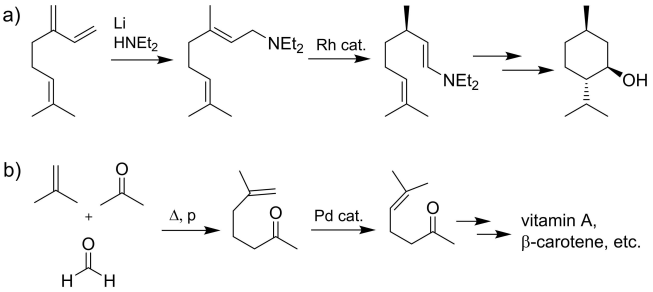

Scheme 1. Industrially relevant olefin isomerization reactions: a) Takasago process and b) BASF synthesis of methyl heptanone.

The discovery of $[Pd^{I}(\mu\text{-Br})(P^{t}Bu_3)]_2$ (**Pd1**)[11] as a highly efficient isomerization catalyst[12] that is mutually compatible with ruthenium metathesis catalysts led to major advances in this field surpassing the efficiency of the Ir/Ag system by Porri[13] and Grubbs,[14] and allowing the valorization of renewable sources.[15] Combinations of **Pd1** with Grubbs- or Hoveyda-type catalysts allow the synthesis of dicarboxylic acid blends from fatty acids,[16] vinylarenes from naturally abundant allylarenes,[17] tsetse-fly attractants from cashew nutshell liquid,[18] and non-estrogenic bisphenol A surrogates from clove oil.[19] They even enable the refining of rapeseed oil methyl ester to biofuel suitable for conventional diesel engines (Scheme 2).[20]

[a] *Prof. Dr. D. Koley, S. De*
Department of Chemical Sciences
Indian Institute of Science Education and Research (IISER)
Kolkata, Mohanpur 741 246 (India)
E-mail: koley@iiserkol.ac.in

[b] *N. Sivendran, Prof. Dr. L. J. Gooßen*
Evonik Chair of Organic Chemistry
Ruhr-Universität Bochum
Universitätsstr. 150, 44801 Bochum (Germany)
E-mail: lukas.goossen@rub.de

Supporting information for this article is available on the WWW under https://doi.org/10.1002/chem.202102554

This manuscript is part of a Special Issue "Cooperative effects in heterometallic complexes".

© 2021 The Authors. Chemistry - A European Journal published by Wiley-VCH GmbH. This is an open access article under the terms of the Creative Commons Attribution Non-Commercial License, which permits use, distribution and reproduction in any medium, provided the original work is properly cited and is not used for commercial purposes.

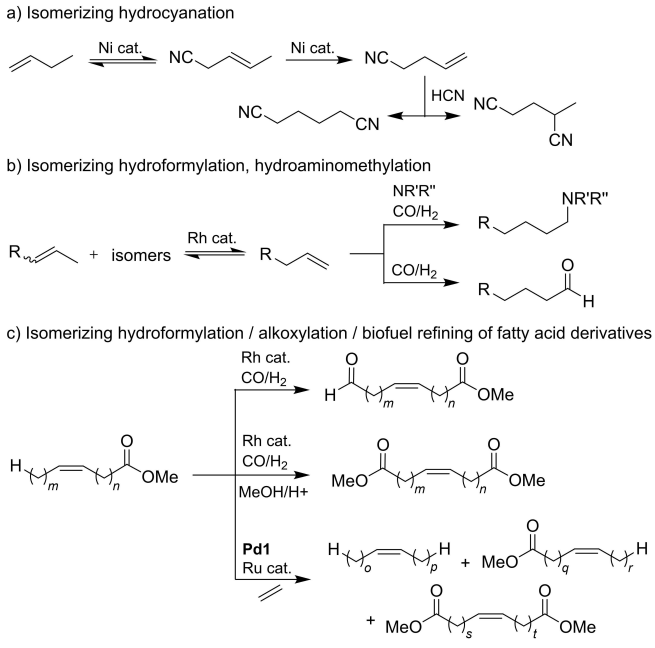

Scheme 2. Isomerizing functionalization processes.

The isomerization activity of the dimeric Pd^{I} complex **Pd1** has been shown to extend to a wide range of substrates including allylic arenes, amides, esters, ethers, and alcohols (Scheme 3).[12] Moreover, **Pd1** isomerizes allyl to vinyl esters, a reaction that has never been reported for other isomerization catalysts. In contrast to bisphosphine Pd complexes, **Pd1** does not only perform single bond flips,[12] but efficiently moves double bonds up and down long carbon chains.[16] Moreover, **Pd1** does not call for strong acids,[21] bases[22] or photochemical

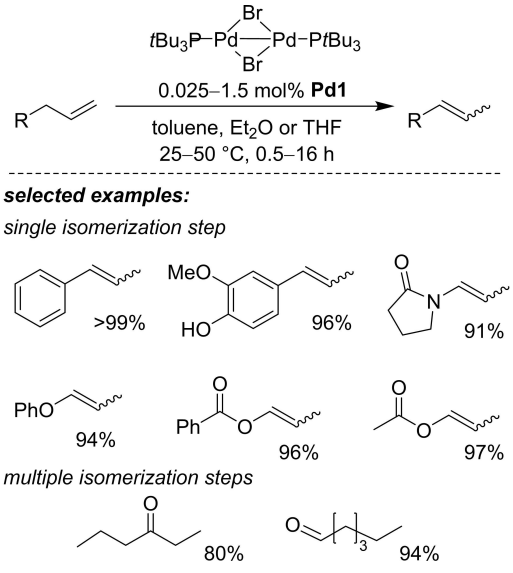

Scheme 3. Pd^{I} as a widely applicable isomerization catalyst.

conditions, which would all be incompatible with sensitive functionalities or olefin metathesis co-catalysts.[23,24]

Computational studies using the strongly simplified model substrate propene (**1a**) revealed that the **Pd1** precatalyst initially undergoes activation through intramolecular C–H activation of the *tert*-butyl ligand.[25] In the course of this step, a reactive dinuclear palladium hydride complex **B1** is formed along with a catalytically inactive palladacycle (**Pd2**) (Scheme 4). The dinuclear Pd–H complex (**B1**) was calculated to mediate double-bond migrations with an energy span of only 9.5 kcal mol^{-1}, which is well below those calculated for other catalysts.[26] Dissociation of the dimeric Pd–H species **B1** involves a considerable additional barrier. It yields an extremely reactive ($PtBu_3$)PdHBr species (**C1**), along with a catalytically inactive dinuclear bispalladacycle (**Pd2**). The Pd species **C1** mediates double-bond migration *via* a *mononuclear pathway*, which has an extremely small energy span of only 5.4 kcal mol^{-1}. In comparison, the *dinuclear pathway* has a slightly larger span, but no additional activation energy is required to reach it from Pd–H species **B1**. The DFT calculations ruled out catalytic cycles starting directly from the Pd^{I} dimer itself.[25]

The main deactivation pathway can only be entered from the *mononuclear pathway*. Two mononuclear Pd species react with each other, liberating a hydrogenation product and regenerating the catalyst precursor $[Pd^{I}(\mu\text{-Br})(P^{t}Bu_3)]_2$.

As the mononuclear catalyst can only be generated with the release of an inert dinuclear palladacycle, each time the deactivation route is taken, the amount of active catalyst is irreversibly reduced. During catalysis, the experimentally observed build-up of catalytically inactive palladacycles is the result of a conversion of the binuclear catalyst **B1** into the short-lived mononuclear Pd–H catalyst **C1**.

Notably, free phosphines are liberated neither during catalyst activation, nor during the catalytic cycles or even catalyst deactivation, which would deactivate the metathesis cocatalysts. The phosphines are trapped in the form of unreactive palladacycles. Whereas the calculations on the model substrate propene thus explained the suitability of $[Pd^{I}(\mu\text{-Br})(P^{t}Bu_3)]_2$ for isomerizing metatheses,[25] important questions concerning the catalytic activity of **Pd1** in more complex isomerization reactions remain: In contrast to propene, the isomerization of most olefins is not degenerate but has a considerable thermodynamic driving force, which must be considered in the calculations, since it may significantly affect catalyst efficiency and longevity. Moreover, the isomerization of most substrates leads to mixtures of *E* and *Z* isomers. The selectivity of their formation under thermodynamic and kinetic conditions should be indicative of the catalyst species involved. Comparison of *E*/*Z* selectivities computed under kinetic conditions with the experimental values might thus allow to pinpoint whether the cooperative dinuclear catalytic cycle or the mononuclear catalytic cycle predominates.

In order to address these key questions, we have now performed in-depth computational studies on the isomerization of various functionalized olefins catalyzed by the dinuclear Pd^{I} species **Pd1**. We have also investigated how the isomerization

© 2021 The Authors. Chemistry - A European Journal published by Wiley-VCH GmbH

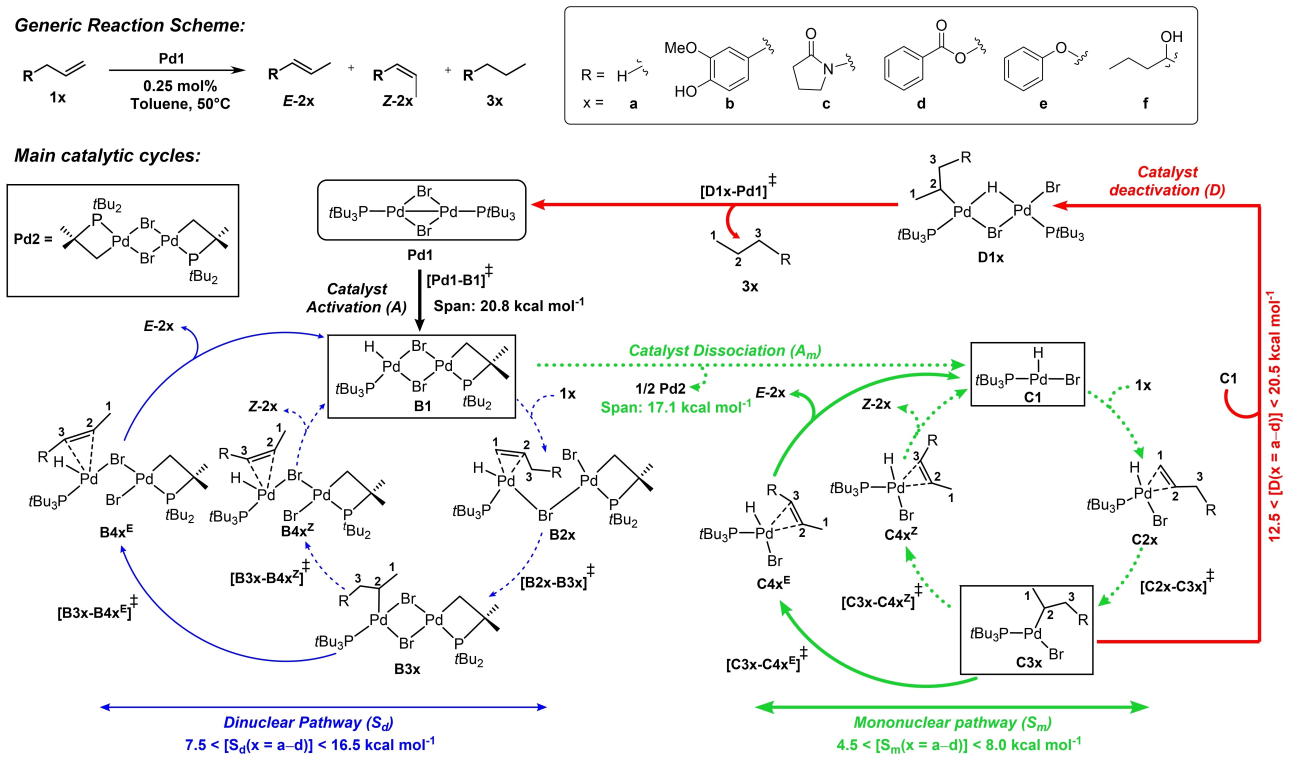

Scheme 4. Overview on the predominant catalytic pathways starting from pre-catalyst **Pd1**.

proceeds in functionalized long-chain alkenes, for which thermodynamic driving forces steer the isomerization process to internal olefins or to conjugated functionalities. In this context, we investigated the isomerization of allylarenes to styrenes (**1 b**), of allyl to vinyl amides (**1 c**), of allyl to vinyl esters (**1 d**) or ethers (**1 e**), and of unsaturated alcohols to aldehydes (**1 f**, **1 g**), both experimentally and theoretically. A particular focus was set on the prediction of the stereochemical outcome.

Computational Details

All calculations were performed with the Gaussian 09 program package.[27] In order to draw comparative conclusions with our previous findings,[25] geometries of all the saddle points were optimized by using the B3LYP exchange-correlation functional[28] including the Grimme empirical dispersion correction D3[29] in conjunction with the 6-31 + G*[30] basis set for all atoms (H, C, N, O, P and Br) except palladium, which was described by using the double-ζ basis set with the relativistic effective core potential of Hay and Wadt (LANL2DZ).[31] The geometries were optimized without any symmetry constraints. Harmonic force constants were computed at the optimized geometries to characterize the stationary points as minima or first-order saddle points. Intermediates and transition states were discerned by the presence of 0 or 1 imaginary frequency, respectively. The rigid rotator harmonic oscillator approximation was applied for evaluating the thermal and entropic contributions that are needed to derive the enthalpies H and Gibbs free energies G at 323.15 K. The transition-state search was carried out by using the linear synchronous transit (LST)[32] method and subsequent optimizations were performed by utilizing the default Berny algorithm incorporated into the Gaussian 09 code.[27] Intrinsic reaction coordinate (IRC) calculations[33] were carried out to authenticate that the transition state connects the corresponding stationary points. In addition, single point calculations were performed at the level of B3LYP-D3/6-311 + + G**(H, C, N, O, P and Br), LANL2TZ(f) Pd using the SMD continuum solvation model[34] implemented in Gaussian09. Toluene (for **1 b**–**e**) and diethyl ether (for **1 f**–**g**) were chosen as a solvent (dielectric constant ε[toluene] = 2.374; ε[diethyl ether] = 4.240) with SMD intrinsic Coulomb radii for the respective atoms.[35] All single point calculations were performed with tight wave function convergence criteria and "ultrafine" (99 950) grid was used in numerical integration. Direct optimization of the structures in the solvent field would have been preferable, but in view of the large number of complex structures that needed to be calculated, we used this more economic approach. It also allowed the comparison of the results with those previously obtained for propene. Concentrations of the reactive species can be obtained by adjusting the pressure value according to the ideal gas law $P_i = RTn_i/V$, where P_i, R, T, n, and V indicate pressure, universal gas constant, absolute temperature, molar quantity, and reaction volume, respectively. The experimental concentrations of catalyst and reactants at the reaction temperature (323.15 K) are approximated by setting the partial pressures of the substrates as follows: olefins (**1 b**–**g**): 1.0×10^{-3} mol = 13.2 atm and of the

© 2021 The Authors. Chemistry - A European Journal published by Wiley-VCH GmbH

intermediates of the catalytic cycle as follows: catalyst (**Pd1**): 2.5×10^{-6} mol = 0.033 atm.[25]

In line with our previous study, we have considered two energy values: $G^{S-L}_{323.15\,K}$ and $H^{S-L}_{323.15\,K}$, which represent the Gibbs free energy and the enthalpy, respectively, in the solution phase at the higher basis set mentioned before. The solution-phase Gibbs free energy was calculated as $G^{S-L}_{323.15\,K}=H^{S-L}_{323.15\,K}-TS^{S-L}_{323.15\,K}$, where $H^{S-L}_{323.15\,K}$ represents the solution-phase enthalpy calculated from $E^{S-L}_{323.15\,K}$ and the enthalpy corrections at the lower basis set, whereas the solvation entropy ($S^{S-L}_{323.15\,K}$) was estimated as $^2/_3$ of the gas phase value.[36] Throughout the text, all bond lengths are given in Angstrom, and relative energies are expressed in kcal mol^{-1}. All energy values are exclusively $\Delta G^{S-L}_{323.15\,K}$, unless otherwise mentioned.

We have also performed noncovalent interaction (NCI) analysis[37] to gain more insights into the important noncovalent interactions present in the stereo-controlling transition states. Topological analysis of the electron density distribution was performed using the wave function generated at the SMD (Toluene)/B3LYP-D3/6-311++G**, LANL2TZ(f) (Pd)//B3LYP-D3/6-31+G*, LANL2DZ (Pd) level of theory. Furthermore, in order to explain the energy barrier of the stereo-controlling transition states, energy decomposition analysis (EDA) calculations according to the methods of Morokuma,[38] Ziegler and Rauk[39] were performed using the SCM-ADF2019.3[40] package. The BP86-D3[41] functional was employed in combination with a triple-ζ-quality basis set using an uncontracted slater-type orbital (STO)[42] augmented with two sets of polarization functions for all atoms without any frozen core approximation. Scalar relativistic effects were treated with the zeroth-order regular approximation (ZORA).[43] In this approach, the activation barrier is partitioned into i) destabilizing distortion of the reactants (ΔE_{dis}) and ii) the stabilizing interaction energy between such distorted reactants (ΔE_{int}). ΔE_{int} is actually composed of four energy terms: ΔE_{elstat}, ΔE_{Pauli}, ΔE_{orb} and ΔE_{disp} and can be represented as $\Delta E=\Delta E_{dis}+\Delta E_{int}=\Delta E_{dis}+(\Delta E_{elstat}+\Delta E_{Pauli}+\Delta E_{orb}+\Delta E_{disp})$. The first term, ΔE_{elstat} denotes the quasi-classical Coulomb interaction energy between the fragments and was calculated by means of the frozen electron density distribution of the fragments in the geometry of the adduct. ΔE_{Pauli} corresponds to the repulsive interactions between the fragments, originating by the fact that two electrons with the same spin cannot occupy the same region in space. Therefore, ΔE_{Pauli} accounts for the destabilizing interaction between the occupied orbitals. In contrast, the stabilizing orbital interaction term ΔE_{orb} represents the interaction between the occupied and virtual orbitals of the two fragments and also elucidates charge transfer and polarization effects. The last term is the dispersion energy ΔE_{disp}. Details of the method, applications and importance of the EDA can be found elsewhere.[44] All figures were generated with the ChemDraw Ultra 16.0 and CYLview visualization software.[45]

In our previous calculations with propene (**1a**) as a model substrate, we had investigated numerous potential catalytic cycles for **Pd1** catalyzed isomerizations. Among them, the pathways depicted in Scheme 4 were by far the most favorable, so that we focused on these for our investigations on the functionalized substrates. The decisive reaction sequences for all derivatives start with the initial catalyst activation (**Pd1**→**B1**, black arrow) followed by a dinuclear isomerization pathway involving Pd-alkyl intermediates **B3x** (blue arrows).[25] The dissociation of the dinuclear Pd–H species **B1** to **C1** provides access to a mononuclear isomerization pathway (green color). The unreactive dinuclear palladacycle **Pd2**, which has experimentally been observed to accumulate in the course of the reaction, forms as a byproduct in this step.

The predominating catalyst deactivation pathway (**C3x**→**Pd1**; red color) starts from mononuclear species. In its course, a hydrogenation product **3x** is released and the original **Pd1** pre-catalyst is regenerated, which can be activated again along the outlined pathway. However, since the mononuclear catalyst can only form with release of an inert dinuclear palladacycle, each time the deactivation route is taken, the amount of active catalyst is irreversibly reduced. The catalyst activation (A = 20.8 kcal mol^{-1}) and the entry to mononuclear route (A_m = 17.1 kcal mol^{-1}) are identical for all substrates, as the substrate is not involved in these steps. In contrast to propene, separate catalytic cycles must be computed for complex substrates, one leading to *E*-, the other to *Z*-configured products. These need to be computed both for the dinuclear and the mononuclear pathway. In the case of unsaturated alcohols, one also has to keep in mind that enol isomers will immediately tautomerize to the corresponding carbonyl compounds, so that the isomerization becomes irreversible.

Experimental Section

The reactions conditions for the isomerization of substrates **1b–g** were optimized for each substrate individually starting from published protocols.[12] The reactions were performed on a 1.0 mmol scale in 2 mL of the respective solvent and were analyzed by GC using *n*-dodecane as standard. In a first set of reactions, the mixtures were stirred until >95% conversion was reached, and the product composition became constant. This way, the product distribution close to the equilibrium was investigated to determine the thermodynamic selectivity. For substrates **1b–e**, a second set of reactions was conducted that was stopped at incomplete conversion of about 50%. This way, the selectivities under kinetic control were investigated.

For eugenol (**1b**), the equilibrium isomerization was performed in the presence of 0.025 mol% of **Pd1** in toluene at 50 °C for 2 h. After this time, the catalyst had lost its reactivity. To achieve kinetic control, the reaction was performed under the same conditions, but stopped after 20 min. For the allyl amide **1c**, the reaction under thermodynamic control was performed in the presence 0.025 mol% **Pd1** in toluene at 50 °C for 16 h, and the reaction under kinetic control was stopped after 2 h. For the allyl ester **1d**, the equilibrium isomerization was performed with 0.25 mol% of **Pd1** in toluene at 25 °C for 24 h. The experiment with kinetic control was stopped after 0.5 h. The equilibrium isomerization of the allyl ether **1e** was performed in the presence of 1.5 mol% **Pd1** in toluene at 50 °C for 18 h. To achieve kinetic control, the reaction was performed analogously, but with only half the amount of catalyst. The alcohols **1e** and **1f** were subjected to isomerization in diethyl ether at 50 °C for 16 h in the presence of 0.25 and 3 mol% of **Pd1** for thermodynamic and kinetic control, respectively. The product distributions were determined by GC analysis using an internal

 © 2021 The Authors. Chemistry - A European Journal published by Wiley-VCH GmbH

standard The conversion was calculated based on the disappearance of starting material relative to the internal standard. The equilibrium is known to be far on the side of the products for all reactions, so that less than 1% starting material are to be expected at full equilibration. The identity of the product was confirmed by NMR analysis after isolation.

Results and Discussion

Isomerization of allyl arenes

The isomerization of eugenol (**1b**) in the presence of 0.025 mol% **Pd1** over two hours furnished a 23:1 mixture of (*E*)- and (*Z*)-isoeugenol at a conversion of 97% (Scheme 5).

Close to the equilibrium, the relative amount of double-bond isomers should correspond to the relative stability of the products. *E*-isoeugenol was calculated to be 2.5 kcal mol^{-1} more stable than *Z*-isoeugenol and 8.4 kcal mol^{-1} more than eugenol. Thus, the equilibrium constant values for *E* and *Z* product formation at 323.15 K can be calculated as 4.2×10^5 (K_E) and 9.1×10^3 (K_Z), respectively. This translates to an equilibrium distribution of **1b**/(*E*)–**2b**/(*Z*)–**2b** = 0.0001:46:1. This correlates well with the experimentally found product distribution and suggests full equilibration was not quite reached over the lifetime of the catalyst. In order to prove this, we subjected the product mixture again for isomerization with fresh catalyst and observed the decrease in the amount of starting material and further increase in the formation of the *E* isomer. This led to a >99% conversion and *E/Z* ratio of 26.6:1, suggesting that even longer time is needed to fully reach equilibrium.

When the reaction was stopped at incomplete conversion, a markedly lower selectivity for the *E*-isomer of 13.8:1 was observed. In order to understand the origin of this kinetic selectivity, we calculated the relevant catalytic pathways for **1b** as outlined in Scheme 4.

The energy profile and energy span of each subsection are compiled in Figure 1. The optimized geometries of reactant, products, intermediates and transition states with selected geometrical parameters are collected in Figure S1 in the Supporting Information.

In the *dinuclear pathway*, the dimeric Pd–H complex **B1** formed in the catalyst activation step initially coordinates to eugenol to form **B2b** in a slightly endergonic process (3.9 kcal mol^{-1}).

The barrier is slightly higher than for the propene model substrate (Figure 1, **B2**→[**B2**–**B3**]‡: 3.0 kcal mol^{-1}). A stabilizing agostic interaction (Figure 2) makes **B3b** more stable by

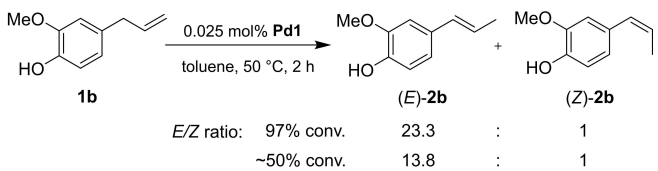

Scheme 5. Isomerization of allyl arene **1b** *via* dinuclear Pd^{I} catalyst **Pd1**.

3.7 kcal mol^{-1} than the π-adduct **B2b**. The conversion of double to single bond in the **1b** fragment is evident from the calculated C^1–C^2 bond lengths in **B3b** and the free allylic arene **1b** (**B3b**/**1b** = 1.509:1.337 Å; Figure S1).

The traditional method to predict the *E/Z* selectivity is to compare the calculated reaction rates based on the difference in activation energies for the selectivity-determining transition states, in this case [**B3b**–**B4b^{E}**]‡ and [**B3b**–**B4b^{Z}**]‡. However, for this unusual profile, in which the selectivity-determining step closely follows a considerably higher barrier, this approach might lead to unrealistically high values.

Thus, as an alternative, we also calculated the reaction rates based on the energy spans of the *E*- and *Z*-selective pathways and derived the predicted product ratio from the difference between these values.

The energy barrier for β-H elimination leading to the *E*-isomerized π-coordinated adduct **B4b^{E}** is lower by 5.5 kcal mol^{-1} ($\Delta\Delta^{\ddagger}G^{S-L}_{323.15\,K}$) than that leading to the *Z* isomer **B4b^{Z}**, which translates into a predicted selectivity of 5437:1 in favor of the *E* product.

The energy spans for (*E*)- and (*Z*)-olefin formation are both calculated using **B1** (2.3 kcal mol^{-1}) as the lowest and [**B2b**–**B3b**]‡ (11.7 kcal mol^{-1}) as the highest energy level. Thus, the alternative reaction pathways have an identical span of 9.4 kcal mol^{-1}, which is in the same range as for propene. Based on the energy span model, one would predict that both stereoisomers are formed with identical rates, which is also conceivable, as the β-H elimination step is not rate-determining within the reaction energy span.

However, this model may underrate the dissipation of energy from the catalyst to the solvent. After crossing the high barrier of the first step, the differences in the lower second step, in which the selectivity is determined, is neglected. In contrast, the model based on the comparison of the selectivity-determining steps does not take into account that these are not rate-determining.

The situation of a selectivity-determining step that is lower in energy than a preceding rate-determining step has been discussed in detail by Hartwig et al. in the context of kinetic isotope effects,[46] and it is experimentally proven that this situation does lead to a significant selectivity, although the energy-span concept would predict otherwise. However, the models treated in the context of KIE cannot be fully matched to the scenario of a stereoselective transformation. We find it reasonable to assume that the true value is somewhere in between the predictions made based on the energy span model and the comparison of the activation energies for the selectivity-determining steps, which is why we went on to calculate both of these values for the two reaction pathways for all substrates.

We have also performed microkinetic modeling based on the energy profiles and calculated the evolution of concentrations over time using the kinetic simulation program COPASI. The results predict that the *E/Z* ratio remains almost unchanged over the time of the reaction, which clearly disagrees with the experimental results. It seems to us that the unusual energy profile causes problems with this method, although it had been

© 2021 The Authors. Chemistry - A European Journal published by Wiley-VCH GmbH

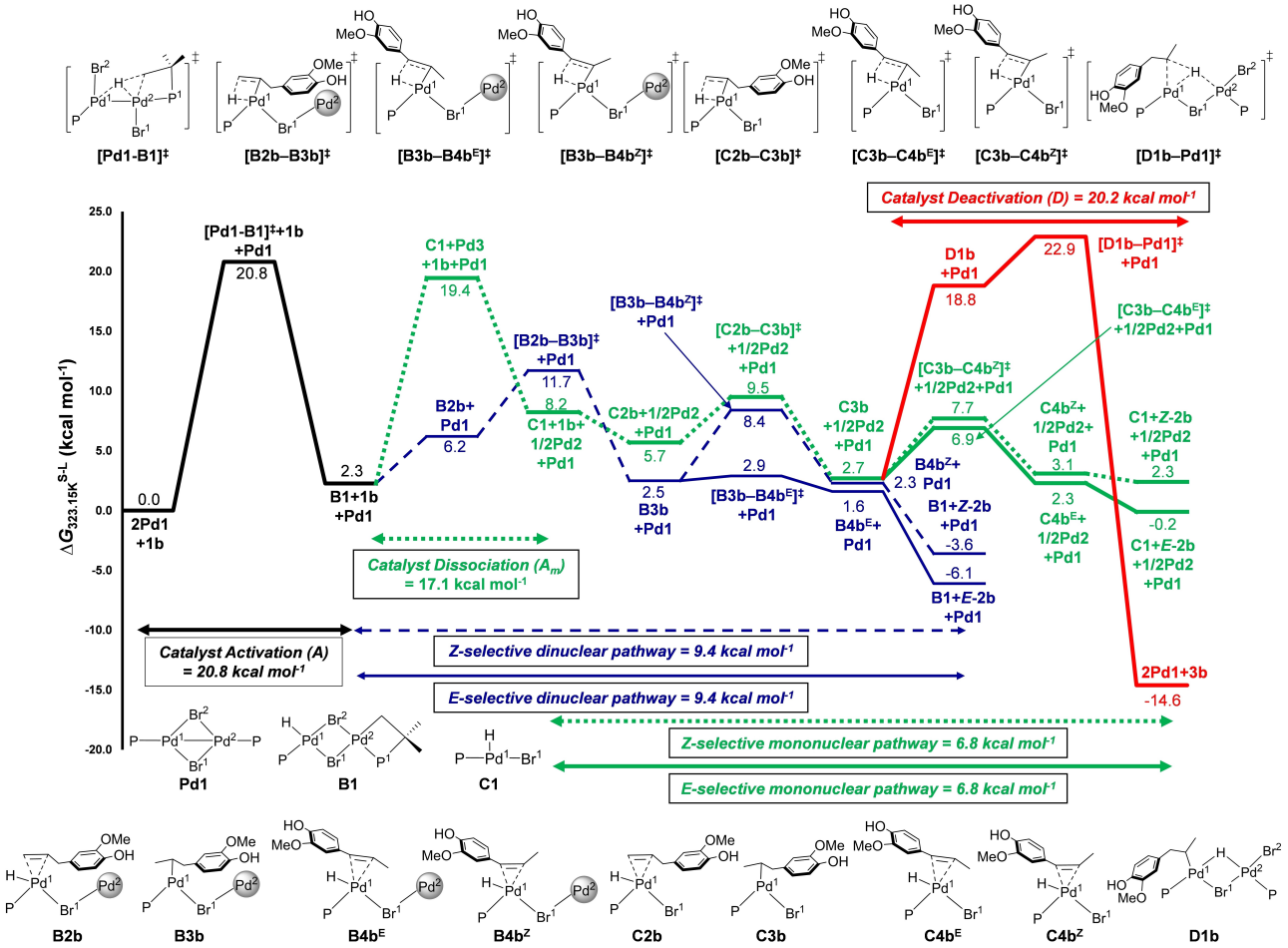

Figure 1. Energy profile for the isomerization of substrate **1 b**. The energy levels are labeled only with the most relevant species; other species included in the energy calculations are omitted for clarity. All energy values ($\Delta G_{323.15\,K}^{S-L}$) are in kcal mol^{-1}.

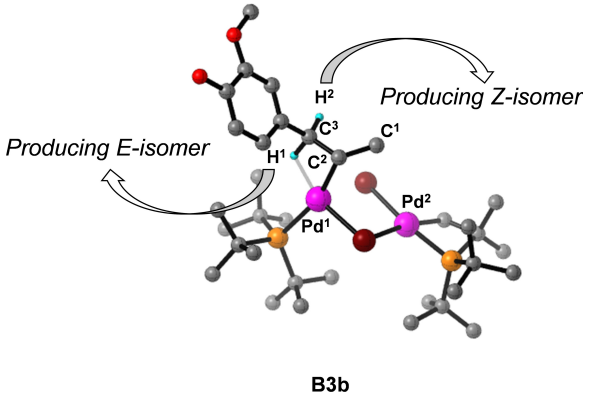

Figure 2. Optimized structure of **B3b** showing an agostic Pd^{1}–H^{1} interaction.

proven to be highly predictive in other cases (Figure S2).[47] Based on the above assessment, we believe that the *dinuclear pathway* is highly *E*-selective, although probably not quite to the extent that the difference between the selectivity-determining transition states would suggest.

Starting from **B1**, the mononuclear Pd–H catalyst **C1** can form along with the unreactive palladacycle **Pd2** *via* an energy barrier of 17.1 kcal mol^{-1}, which sets the stage for the alternative *mononuclear pathway* (Figure 1). It is reasonable to assume that under conditions that allow crossing the 20.8 kcal mol^{-1} barrier for pre-catalyst activation, part of the catalyst will find sufficient energy to also overcome this additional barrier and enter the *mononuclear pathway*. The alkene coordination is exergonic in this case (**C1** + **1 b** → **C2b**; $\Delta G_{323.15\,K}^{S-L} = -2.5$ kcal mol^{-1}), and the insertion of the olefin into the Pd–H bond ([**C2b**–**C3b**]‡) constitutes the highest barrier in absolute terms with 9.5 kcal mol^{-1}. Similar to the dinuclear pathway, the subsequent β-H eliminations *via* [**C3b**–**C4b^{E}**]‡ or [**C3b**–**C4b^{Z}**]‡, leading to the *E* and the *Z* product, both have lower barriers. However, as the energy difference between **C2b** (5.7 kcal mol^{-1}) and [**C2b**–**C3b**]‡ (9.5 kcal mol^{-1}) is smaller than the differences between **C3b** (2.7 kcal mol^{-1}) and [**C3b**–**C4b^{E}**]‡ (6.9 kcal mol^{-1}) or [**C3b**–**C4b^{Z}**]‡ (7.7 kcal mol^{-1}), the energy span is now calculated from the latter values, since this is an exergonic reaction. Thus, the energy span for the formation of the *Z* product is 5.0 kcal mol^{-1}, that is, only 0.8 kcal mol^{-1} larger

© 2021 The Authors. Chemistry - A European Journal published by Wiley-VCH GmbH

than for the *E* product (4.2 kcal mol^{-1}). This is slightly smaller than the span calculated for propene (5.4 kcal mol^{-1}).

The difference in energy spans translates to a predicted *E*/*Z* ratio of only 3.4:1 under kinetic conditions. The same value is obtained when calculating the rates from the difference in the activation energy of the selectivity-determining transition states of β-hydride elimination ([**C3b**–**C4b^{E}**]‡ and [**C3b**–**C4b^{Z}**]‡). Considering that the activation energies for β-H eliminations are lower than for olefin insertion, and that the energy might not fully dissipate after each step, one might argue that the *E*/*Z* selectivity would probably be even lower than the calculated 3.4:1 if the reaction followed predominantly the mononuclear pathway.

Catalyst deactivation starts from the monomeric cycle and involves an endergonic adduct formation between **C1** and **C3b** ($\Delta G^{S-L}_{323.15\,K}$ = 16.1 kcal mol^{-1}) and formation of the bridging Pd–H–Pd intermediate **D1b**. Its overall energy span of 20.2 kcal mol^{-1} is similar to that calculated for propene and in the same range as the barrier for the catalyst activation. This corresponds well with the experimental finding that **Pd1** is a highly active catalyst for the isomerization of eugenol, but is relatively short-lived.

Overall, the experimentally observed relatively high *E*/*Z* ratio of 13.8:1 at incomplete conversion is best explained if both the dinuclear and the mononuclear pathway are involved. This appears reasonable, since only a moderate barrier separates both pathways, and both have sufficiently small energy spans.

Isomerization of allyl amides, esters and ethers

Next the isomerization of allyl amides, esters and ethers were investigated both under near-equilibrium conditions and kinetic control.

The isomerization of *N*-allyl-2-pyrrolidone (**1 c**) in the presence of 0.025 mol% **Pd1** over 16 h furnished a 49:1 mixture of (*E*)- and (*Z*)-vinyl amide at a conversion of 96% (Scheme 6). As (*E*)-2-propenylamide was calculated to be more stable by 3.4 kcal mol^{-1} than the *Z* isomer and by 9.0 kcal mol^{-1} than the starting material **1 c**, the equilibrium constants for *E* and *Z* product formation are predicted to be 1.2×10^{6} (K_E) and 6.0×10^{3} (K_Z) at 323.15 K. This translates to a ratio of **1 c**/(*E*)-**2 c**/(*Z*)-**2 c** of $<$0.0002:198:1. When the reaction was stopped at incomplete conversion, a much lower selectivity for the *E*-isomer in a ratio of 10:1 was observed.

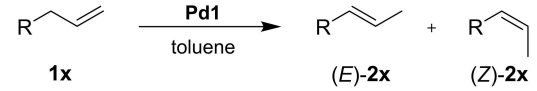

1x (*E*)-**2x** (*Z*)-**2x**

E/*Z* ratio:				
Y = *N*-2-pyrrolidone (**1c**)	96% conv.	48.5	:	1
	~50% conv.	10	:	1
OCOPh (**1d**)	98% conv.	1	:	2.2
	~50% conv.	1	:	2
OPh (**1e**)	95% conv.	1	:	2.8
	~50% conv.	1	:	26.5

Scheme 6. Isomerization of allyl amide **1 c**, allyl ester **1 d** and allyl ether **1 e** by dinuclear Pd^{I} catalyst **Pd1**.

The catalytic isomerization of allyl benzoate (**1 d**) required a larger amount of catalyst (0.25 mol%) and longer reaction time (24 h) to reach near-quantitative conversion (98%), yielding the *Z*-stereoisomer as major product (*E*/*Z* = 1:2.2, Scheme 6). This is in line with the stability calculated for (*Z*)-2-propenyl benzoate, which is 0.4 kcal mol^{-1} more stable than (*E*)-2-propenyl benzoate, and 5.9 kcal mol^{-1} more stable than **1 d**. This translates to equilibrium constants for *E* and *Z* product formation of 4.8×10^{3} (K_E) and 9.6×10^{3} (K_Z) at 323.15 K, corresponding to a **1 d**/(*E*)-**2 d**/(*Z*)-**2 d** ratio of 0.0002:1:2.0. At incomplete conversion, almost the same *E*/*Z* selectivity of 1:2 was observed.

The isomerization of allyl phenyl ether (**1 e**) required a remarkably high loading of 1.5 mol% **Pd1** to proceed to completion. Over 18 h, a conversion of 95% was reached, yielding a 1:2.8 mixture of (*E*)- and (*Z*)-vinyl ethers (Scheme 6). Thus, similarly to the allyl ester, the allyl ether **1 e** also reacts with preferential formation of *Z* products. The (*Z*)-2-propenyl ether (*Z*)-**2 e** was calculated to be slightly more stable (−0.6 kcal mol^{-1}) than (*E*)-2-propenyl ether (*E*)-**2 e** and 7.5 kcal mol^{-1} more stable than the allyl phenyl ether (**1 e**). The calculated equilibrium constants for *E* and *Z* product formation are 4.5×10^{4} (K_E) and 1.1×10^{5} (K_Z) respectively at 323.15 K, which translates to a predicted ratio of **1 e**/(*E*)-**2 e**/(*Z*)-**2 e** = 0.00002:1:2.4. At incomplete conversion, a much higher *E*/*Z* selectivity for the *Z* product of 1:27 was observed.

In order to rationalize these findings, the reaction profiles were calculated for the isomerization of **1 c–e** and are depicted as simplified overlay in Figure 3. The detailed energy profiles and optimized geometries of reactant, products, intermediates and transition states with selected geometrical parameters are collected in Figures S3–S8.

For the allyl amide **1 c** (Figure S3), the energy spans for the formation of the isomeric products along the *dinuclear pathway* are determined by the difference of **B1** (2.3 kcal mol^{-1}) and [**B3c**–**B4c^{E}**]‡ (12.0 kcal mol^{-1}) or [**B3c**–**B4c^{Z}**]‡ (18.7 kcal mol^{-1}), respectively. The difference of 6.7 kcal mol^{-1} should translate into a high selectivity for the *E* substrate amounting to *E*/*Z* = 35742:1. Comparing the difference in the activation energies of the selectivity-determining transition states [**B3c**–**B4c^{E}**]‡ (12.0 kcal mol^{-1}) with [**B3c**–**B4c^{Z}**]‡ (18.7 kcal mol^{-1}) for the β-H elimination step also predicts an almost exclusive formation of (*E*)-enamide product (*E*)-**2 c** under kinetic conditions, if the reaction followed the dinuclear pathway.

Within the *mononuclear pathway*, the migratory insertion is rate-determining, resulting in the same energy span of 5.9 kcal mol^{-1} for the *E*- and *Z*-selective pathway from **C2c** (7.4 kcal mol^{-1}) and [**C2c**–**C3c**]‡ (13.3 kcal mol^{-1}). Based on the energy span concept, no preference for either stereoisomer under kinetic conditions is expected. Based on the comparison of the selectivity-determining transition states [**C3c**–**C4c^{E}**]‡ (12.6 kcal mol^{-1}) and [**C3c**–**C4c^{Z}**]‡ (13.0 kcal mol^{-1}), a small *E*/*Z* ratio of 1.7:1 is predicted. In summary, both models predict that the *E*/*Z* ratio at incomplete conversion would be very small if the reaction followed the mononuclear pathway exclusively.

 © 2021 The Authors. Chemistry - A European Journal published by Wiley-VCH GmbH

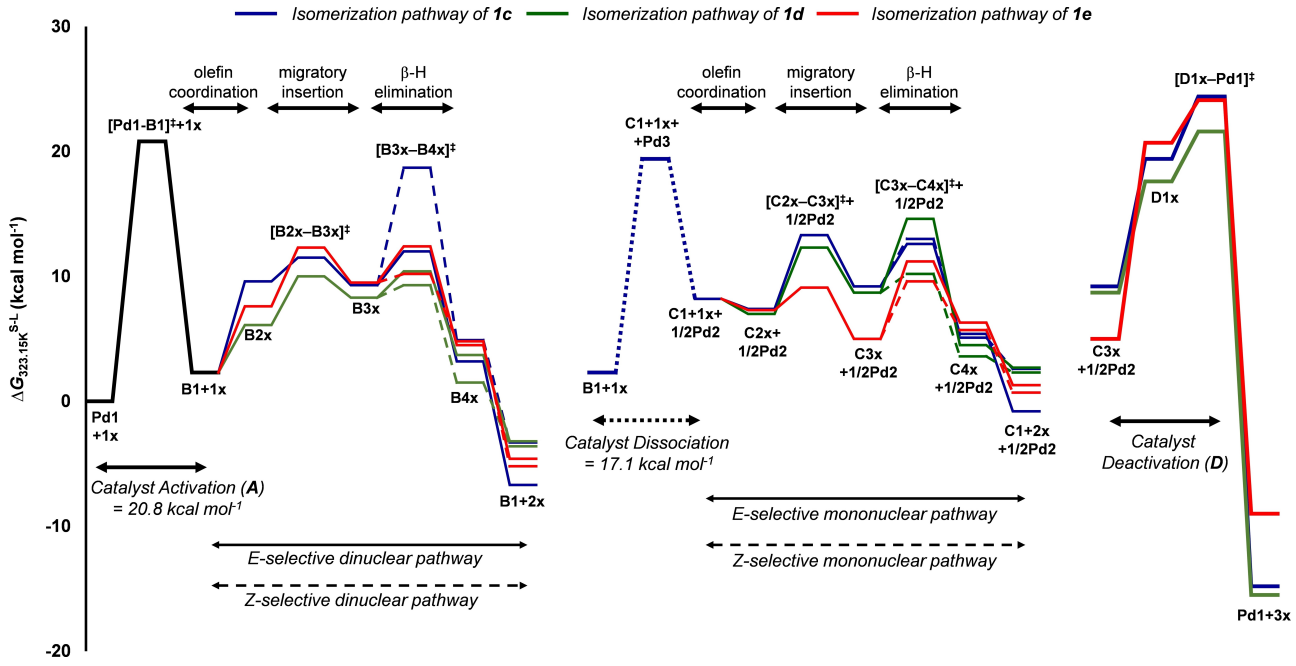

Figure 3. Overlay of all the substrates **1 c**–**e**. The energy levels are labeled only with the most relevant species; other species included in the energy calculations are omitted for clarity.

Experimentally, a moderate 10:1 *E/Z* selectivity was observed under kinetic conditions, which is best explained by a participation of both pathways. This is a very conceivable scenario: There is only a moderate barrier between the highly selective dinuclear pathway with its reasonable energy span, and the nonselective mononuclear pathway, which has an even smaller span, and is separated from catalyst deactivation by a substantial energy barrier.

In the case of the allyl ester **1 d** (Figure S5), the energy span for the *E*-selective, *dinuclear pathway* is calculated from **B1** (2.3 kcal mol^{-1}) and [**B3d**–**B4d**^{E}]$^{+}$ (10.4 kcal mol^{-1}) as 8.1 kcal mol^{-1}. For the corresponding *Z*-selective pathway, a span of 7.7 kcal mol^{-1} is calculated between **B1** (2.3 kcal mol^{-1}) and [**B2d**–**B3d**]$^{+}$ (10.4 kcal mol^{-1}). Based on the difference of 0.4 kcal mol^{-1}, one would expect a preference of the *Z* versus the *E* isomer of 1.9:1.

From the energy difference of the two selectivity determining transition states [**B3d**–**B4d**^{E}]$^{+}$ (10.4 kcal mol^{-1}) and [**B3d**–**B4d**^{Z}]$^{+}$ (9.3 kcal mol^{-1}), one would predict a ratio of 5.3:1. Thus, along the dinuclear pathway, formation of the *Z* isomer is slightly favored not only thermodynamically but also kinetically.

For the *mononuclear pathway*, the *E*-selective pathway has an energy span of 7.6 kcal mol^{-1} between **C2d** (7.0 kcal mol^{-1}) as lowest and the β-H elimination [**C3d**–**C4d**^{E}]$^{+}$ (14.6 kcal mol^{-1}) as highest energy level. In contrast, the energy span for the *Z*-product is calculated from the difference between **C2d** (7.0 kcal mol^{-1}) and the migratory insertion step [**C2d**–**C3d**]$^{+}$ (12.3 kcal mol^{-1}). One would expect a high kinetic preference of the *Z* over *E* isomer of 36:1, whereas the difference between the selectivity-determining transition states [**C3d**–**C4d**^{Z}]$^{+}$ (10.2 kcal mol^{-1}) and [**C3d**–**C4d**^{E}]$^{+}$ (14.6 kcal mol^{-1}), translates to a high *E/Z* ratio of 1:922.

As the experimentally observed *E/Z* ratio under kinetic conditions is only 1:2, the reaction must proceed mostly according to the dinuclear rather than the mononuclear pathway. A potential explanation for this arises from the assessment of catalyst deactivation. It has a span of only 12.9 kcal mol^{-1} for allyl ester **1 d**, which is the smallest of all investigated substrates. The small span is a result not only of the high energy level of its entry point at **C3d**, but also of the stabilization of the deactivation transition state [**D1d**–**Pd1**]$^{+}$ (Figure S5). This is primarily due to stabilizing C–H···π and C–H···O interactions, that are absent in the transition states of the other substrates. Furthermore, due to the exceptionally low deactivation span for the mononuclear pathway, the catalyst is likely to decompose rapidly, rather than achieving high turnover *via* the highly selective mononuclear pathway. Thus, the less selective dinuclear pathway predominates and leads to a overall low *E/Z* selectivity.

For the allyl ether **1 e** (Figure S7), the energy span along the *dinuclear pathway* for the *E* isomer is calculated from the difference between **B1** (2.3 kcal mol^{-1}) and [**B3e**–**B4e**^{E}]$^{+}$ (12.4 kcal mol^{-1}), whereas the energy span for the *Z*-isomer results from the difference between **B1** (2.3 kcal mol^{-1}) and [**B2e**–**B3e**]$^{+}$ (12.3 kcal mol^{-1}). Thereby, an *E/Z* ratio of 1:1.2 is predicted, while by comparison of the selectivity-determining transition states [**B3e**–**B4e**^{E}]$^{+}$ (12.4 kcal mol^{-1}) and [**B3e**–**B4e**^{Z}]$^{+}$ (10.2 kcal mol^{-1}), a high *E/Z* selectivity of about 1:32 is calculated.

Along the *mononuclear pathway* for the ether **1 e**, β-hydride elimination is rate determining both for the *E* and *Z* product

© 2021 The Authors. Chemistry - A European Journal published by Wiley-VCH GmbH

formation. This results in energy spans of 6.2 kcal mol^{-1} for the *E*-selective and 4.6 kcal mol^{-1} for the *Z*-selective pathway from **C3e** (5.0 kcal mol^{-1}) as lowest and [**C3e**–**C4e**^{X}]$^{+}$ as highest energy level (11.2 kcal mol^{-1} and 9.6 kcal mol^{-1}, respectively) and a kinetic *E*/*Z* selectivity of about 1:13, which is identical to when the transition states are compared.

Experimentally, the *E*/*Z* selectivity is markedly higher under kinetic (26.5:1) than thermodynamic conditions (2.2:1). Once again, this is best explained with the participation of both catalytic pathways, since the experimentally observed selectivity is in between the values calculated for the dinuclear and the mononuclear pathway.

The catalyst deactivation with an energy span of 19.1 kcal mol^{-1} is in the same range as for propene. However, these calculations do not offer an explanation, why the catalyst has to be employed in such high loading for this particular substrate. The span of the dinuclear pathway is only slightly higher than for other substrates, and the mononuclear pathway is in the usual range.

Origin of the kinetic stereoselectivity

In order to probe the origin of stereo-controlling transition states, we have employed noncovalent interaction (NCI) plots which are based on the topological distributions of electrons.[37,48] As both the isomerization routes (*dinuclear and mononuclear pathway*) follow a similar trend for all the substrates (**1b**–**e**), NCI plots for the stereo-controlling transition states in case of dinuclear pathway are collected in Figure S9. In the graphical presentation of NCI plots, strong attractive interactions display as blue regions whereas dispersion or weak noncovalent interactions as green regions, and red as repulsive interactions. In the lower energy transition states, C–H···π interaction as well as π···π interactions are found to be more effective. The higher the number of such interactions, the greater the stabilization of the stereo-controlling transition state.[49] For example, the more stable transition state [**B3b**–**B4b**^{E}]$^{+}$ (Figure S9a), exhibits a greater number of C–H···π interactions (2 *vs.* 1) than in the relatively unstable transition state [**B3b**–**B4b**^{Z}]$^{+}$.

C–H···O and C–H···π interactions also contribute to the energy differences between the transition states. Thus for the allylic amide substrate **1c**, the number of C–H···O interactions are higher (2 *vs.* 1) for transition state [**B3c**–**B4c**^{E}]$^{+}$ than in [**B3c**–**B4c**^{Z}]$^{+}$ (Figure S9b). In a similar fashion, for the remaining substrates **1d** and **1e**, the number of C–H···O and C–H···π interactions are predominant in *Z*-controlling transition states (2:1 *vs.* 1:1 in [**B3d**–**B4d**^{Z}]$^{+}$ and [**B3e**–**B4e**^{Z}]$^{+}$) than its corresponding stereo-variant transition states (Figure S9c and d). These interactions lead to differential stabilization of the stereo-controlling transition states.

We also performed a fragment-based energy decomposition analysis (EDA) in order to explain the differential energy barriers in stereo-controlling transition states for substrates **1b**–**e** along the *dinuclear pathway* (Table S1).[50] If we consider the stereo-controlling transition states of **1b**, the calculated results show that the distortion energy (ΔE_{dis}) is higher in [**B3b**–**B4b**^{Z}]$^{+}$ (34.6 kcal mol^{-1}) than in [**B3b**–**B4b**^{E}]$^{+}$ (27.6 kcal mol^{-1}), and this originates mainly from the distortion of the substrate in the transition states ($\Delta E_{d}(2) = 5.3$ kcal mol^{-1} in [**B3b**–**B4b**^{E}]$^{+}$ *vs.* 11.3 kcal mol^{-1} in [**B3b**–**B4b**^{Z}]$^{+}$; Table S1). Interestingly, for **1b**, the difference in the total EDA energies between the transition states is exactly the same with the difference in their activation barriers ($\Delta\Delta^{+}G^{S-L}_{323.15\,K} = 5.5$ kcal mol^{-1}). Though it may not be true for other substrates the trend in relative stabilities holds. For substrate **1c**, the *E*-selective pathway is favorable over the *Z*-selective pathway predominantly due to the interaction energy (ΔE_{int}), which overcomes the destabilizing distortion energy (ΔE_{dis}). The reversal in stereoselective outcome is also quite clear from the ΔE_{int} values of the stereo-controlling transition states for **1d** and **1e** (Table S1), despite, the total distortion energies for *E*-/*Z*-controlling transition states are quite similar ([**B3d**–**B4d**^{E}]$^{+}$/[**B3d**–**B4d**^{Z}]$^{+}$ = 36.0/36.3 kcal mol^{-1} and [**B3e**–**B4e**^{E}]$^{+}$/[**B3e**–**B4e**^{Z}]$^{+}$ = 40.0/40.4 kcal mol^{-1}). Overall, the interaction energy plays an important role in controlling the kinetic *E*/*Z* selectivity.

Isomerization of allyl alcohols

In contrast to the prior discussed substrates, allyl alcohols do not result in *E* or *Z* isomers of the respective olefins, but undergo keto-enol tautomerization after isomerization to an aldehyde or ketone depending on the nature of the enol.

In the presence of 0.25 mol% **Pd1**, the secondary alcohol hexen-3-ol (**1f**) is converted to the corresponding ketone by double bond migration and subsequent tautomerization in 98% over 16 h (Scheme 7).

The calculated energy profile for the isomerization of **1f** is depicted in Figure 4. The optimized structures of the numerous intermediates and transition states along with their key structural parameters are presented in Figures S10.

In the *dinuclear pathway*, generation of the π-coordinated **B2f** complex occurs in the known fashion with coordination of the terminal C^1=C^2 bond of **1f** to the catalytic species **B1**. Migratory insertion of the coordinated alkene into the Pd^1–H bond forms intermediate **B3f** accompanying a low barrier of 6.6 kcal mol^{-1}. In fact, this barrier is the lowest among the corresponding routes (**B1**→**B3f**) computed for all other substrates. Subsequently, from complex **B3f**, the β-H elimination takes place *via* transition state [**B3f**–**B4f**]$^{+}$ to give a π-coordinated complex **B4f**. This process is very facile with **B4f** lying 6.2 kcal mol^{-1} lower than **B3f** in the energy surface. From here, facile de-coordination of the isomeric alcohol species **2f′** occur that immediately undergoes keto-enol tautomerism to

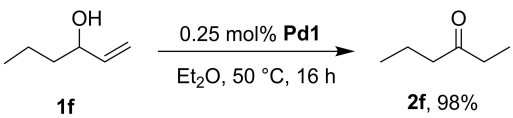

Scheme 7. Isomerization of allyl alcohol **1f** *via* dinuclear Pd^{I} catalyst **Pd1**.

 © 2021 The Authors. Chemistry - A European Journal published by Wiley-VCH GmbH

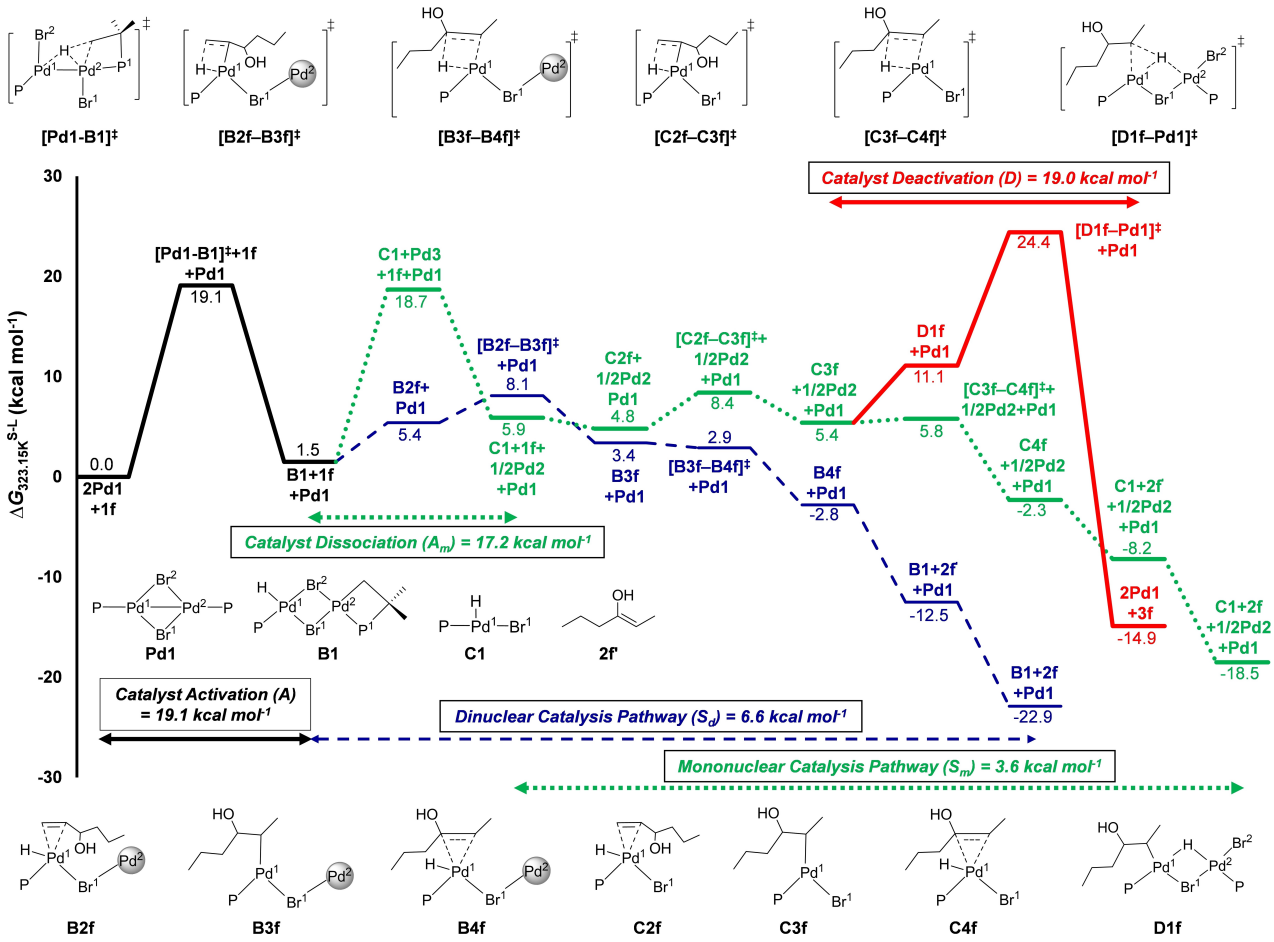

Figure 4. Energy profile for the isomerization of substrate **1f**. The energy levels are labeled only with the most relevant species; other species included in the energy calculations are omitted for clarity. All energy values ($\Delta G^{S-L}_{323.15K}$) are in kcal mol^{-1}.

furnish the hexane-3-one product **2f**. The calculated rate constant value (k_e) of 2.3×10^8 sec^{-1} corresponding to an energy span of only 6.6 kcal mol^{-1} along with product stabilization of −24.4 kcal mol^{-1}, indicates a favorable outcome of the reaction under both kinetic and thermodynamic grounds.

In a similar fashion, the *mononuclear pathway* initiates with the coordination of the substrate to **C1** leading to a stable π-coordinated complex **C2f** ($\triangle G^{S-L}_{323.15K} = -1.1$ kcal mol^{-1}; Figure 4). Thereafter, migratory insertion occurs *via* transition state [**C2f**–**C3f**]‡ accompanying a barrier of 3.6 kcal mol^{-1} and leading to Pd-alkyl intermediate **C3f**. Next, a facile β-H elimination ($\Delta^{\ddagger} G^{S-L}_{323.15K} = 0.4$ kcal mol^{-1}) proceeds to give **C4f**, where the C=C bond weakly coordinates to Pd^{I} center. The isomeric alcohol **2f'**, which later rearranges to **2f**, liberates instantaneously with the generation monomeric Pd-hydride catalyst **C1**.

The *catalyst deactivation* proceeds with an endergonic combination (5.7 kcal mol^{-1}) of **C3f** with **C1** to generate **D1f**. The deactivation span is reasonably large (19.0 kcal mol^{-1}) but what draws our attention is the facile monomeric product formation route from **C3f**→**C1** + **2f**, entailing a nominal barrier of only 0.4 kcal mol^{-1} (**C3f**→**C4f**). In addition, the high exergonic liberation of **2f** drags the reaction course towards the final β-H elimination route.

We next investigated the isomerization of the primary alcohol hex-5-en-1-ol (**1g**) to hexanal (**2g**) as an example of a double bond migration over several carbon atoms. The reaction was experimentally found to proceed in 94% yield using a relatively high loading of 3 mol% **Pd1** over 16 h (Scheme 8).

Isomerization events along the alkyl chain under both mononuclear and dinuclear catalytic systems and the deactivation are schematically depicted in Figure 5. Correspondingly, the detailed energy profile and the optimized structures of the saddle points, including the relevant structural parameters are collected in Figures S11 and S12.

The initiation of the *dinuclear pathway* occurs with the coordination of **1g** with **B1** to provide the π-coordinated intermediate **B2g**. Thereafter, migratory insertion of [**Pd1**-H] takes place in a similar manner as other substrates giving rise to the Pd-alkyl species **B3g**, which is 6.3 kcal mol^{-1} less stable than

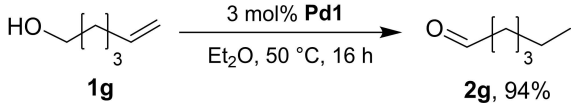

Scheme 8. Isomerization of allyl alcohol **1g** *via* dinuclear Pd^{I} catalyst **Pd1**.

© 2021 The Authors. Chemistry - A European Journal published by Wiley-VCH GmbH

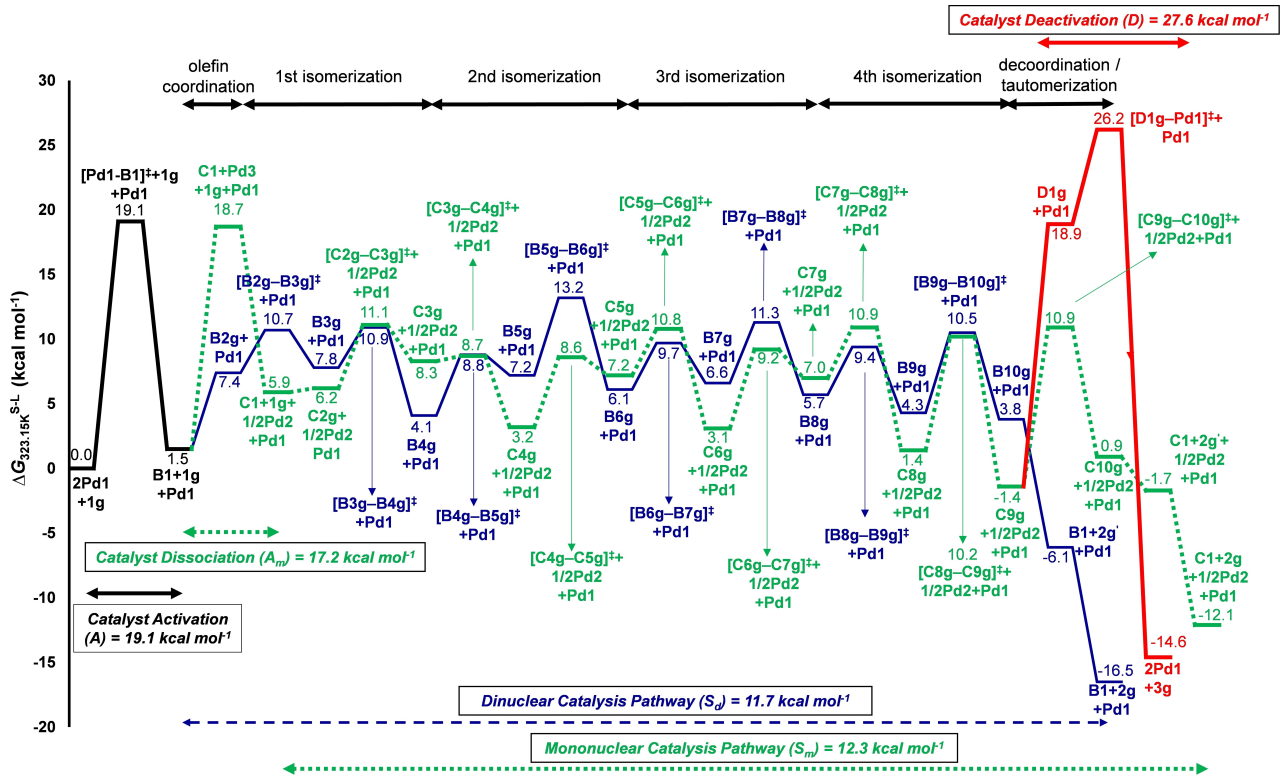

Figure 5. Simplified energy profile diagram for the isomerization of substrate **1 g**. The energy levels are labeled only with the most relevant species; other species included in the energy calculations are omitted for clarity. All energy values ($\Delta G^{S-L}_{323.15\,K}$) are in kcal mol^{-1}.

B1 and is accessible after surmounting a barrier of 9.2 kcal mol^{-1} (**B1**→[**B2g**–**B3g**]‡). β-Hydride elimination from **B3g** will afford C^2=C^3 coordinated intermediate **B4g**, which is 3.3 kcal mol^{-1} more stable than the starting π-complex **B2g**. A series of similar migratory insertions and β-hydride eliminations transfer the olefin bond along the alky chain until it reaches the hydroxy group in **B10g**. Facile de-coordination of the enol affords **2 g′**, which tautomerizes to hexanal **2 g**. The energy span for this dinuclear pathway is 11.7 kcal mol^{-1}, with the highest transition state residing between the step **B5g**→**B6g** and a calculated rate constant (k_g) of 7.7×10^4 s^{-1}. The irreversible nature of the reaction is supported by the highly exergonic (−18.0 kcal mol^{-1}) formation of hexanal (**2 g**).

The *catalyst deactivation* can originate from any one of the numerous Pd-alkyl complexes but we decided to initiate the **C1** addition from the most stable intermediate **C9g**. The deactivation energy span is 27.6 kcal mol^{-1}, which is the largest among all the similar routes for other substrates. In comparison to the previous substrate **1 f**, which furnishes a secondary enol, for **1 g** the double bond migration events end at a terminal -OH group, and the elimination of the product seems to be particularly difficult with a mononuclear catalyst (Figure 5). Nonetheless the difference in relative transition state stabilities among the deactivation and the final β-H elimination paths is 15.3 kcal mol^{-1}, which is well within the range for other substrates (11.0 kcal mol^{-1} $< \Delta\Delta^{\ddagger}G^{S-L}_{323.15\,K} >$ 19.0 kcal mol^{-1}).

For this particular substrate, the dinuclear pathway is clearly more effective than the mononuclear pathway, which is remarkable, as it has a larger span for all other substrates. This may be one reason why such a high catalyst loading is required in this case.

Conclusion

A combined experimental and computational study of the isomerization activity of the dinuclear Pd^{I} complex **Pd1** towards various functionalized olefins has provided new insights into the cooperative action of the two palladium centers. Comparative assessment of the energy profiles for the catalyst activation, the dinuclear, and the mononuclear pathways for double-bond isomerization as well as catalyst deactivation has provided values that are in good agreement with the experimental results with regard to the activity and longevity of the Pd^{I} catalyst. The experimentally observed *E*/*Z* selectivities at high conversion correspond well with the calculated equilibrium values, thus confirming that the reactions are not far from full equilibration. In comparison to the experimentally observed product distributions, the calculated values predict even lower concentrations of the starting materials after full equilibration. Control experiments indicate that the catalyst lifetime is still insufficient to lead the isomerizations to full equilibrium, although >95% conversion was usually reached.

© 2021 The Authors. Chemistry - A European Journal published by Wiley-VCH GmbH

A comparison of the experimentally observed *E*/*Z* ratios at incomplete conversion with the calculated kinetic selectivities turned out to be a valuable tool for assessing the relative contribution of the di- and mononuclear pathways to product formation. In previous investigations, in which simple propene served as the model olefin, it was found that the mononuclear pathway can only be accessed over a high barrier, but has a substantially smaller energy span than the dinuclear pathway. Thus, it had appeared reasonable to assume that most of the product is formed *via* the mononuclear pathway.[25]

Investigations into functionalized substrates that lead to mixtures of stereoisomers have now permitted a comparison of the experimental *E*/*Z* ratio at incomplete conversion with the values calculated for the competing mono- and dinuclear pathways. In order to explain the experimentally observed selectivities, a substantial amount of product must have formed *via* the dinuclear pathway. Thus, the catalyst is likely to pass multiple times through the dinuclear pathway, in which the isomerization is cooperatively promoted by two palladium centers, before it eventually dissociates. The resulting monometallic Pd species then enters the highly effective mononuclear pathway, which, however, has a low barrier towards catalyst deactivation.

For eugenol **1b**, the *E*/*Z* selectivities for the mononuclear pathway were predicted to be substantially lower than those observed experimentally. This leads to the conclusion that the high *E*/*Z* ratios are caused by the contribution of the dinuclear pathway, which was calculated to be highly *E*-selective for this substrate. For the allyl benzoate **1d**, the experimentally observed *E*/*Z* value was in a medium range, but the mononuclear pathway was predicted to be extremely stereoselective. Thus, a substantial amount of product must have formed *via* the dinuclear pathway, which was calculated to be non-stereoselective for this substrate.

Overall, these investigations show that, despite its somewhat larger energy span, the dinuclear pathway with its cooperative action of two palladium contributes more strongly to product formation than previously proposed.[25]

The energy profiles for some products are unusual in that a rate-determining insertion precedes the selectivity-determining β-H elimination. If the rate-determining step is also selectivity-determining, the Curtin-Hammett principle allows a straightforward calculation of the selectivity. However, if the selectivity is determined in a step that immediately follows a higher barrier, the reaction might not display steady-state behavior. If the selectivity is calculated from the energy difference between activation energies of the selectivity-determining steps, the values might get unrealistically high. In such cases, a comparison of reaction rates calculated from the energy spans of the competing reaction was also performed. However, in the case of an energetically unfavorable first rate-determining step followed by a lower selectivity-determining barrier, the energy span concept neglects the influence of the latter, predicting a non-selective reaction. It is reasonable to assume that the experimental values will be somewhere in between these extremes, and this is what we observed. Further research is clearly required to find out how these two complementary models, neither of which seems fully applicable to the given case, can be adapted to this kind of reaction profile.

Acknowledgements

Funded by the Deutsche Forschungsgemeinschaft (DFG, German Research Foundation) under Germany's Excellence Strategy: EXC-2033-390677874-RESOLV and SFB TRR88 "3MET" as well as the bilateral DST-DFG scheme (INT/FRG/DFG/P-05/2017/GO 853/12-1). We thank IISER Kolkata for the computational facility, BMBF and the state of NRW (Center of Solvation Science "ZEMOS"), as well as the UGC, India for a Senior Research Fellowship to S.D. and the Fonds der chemischen Industrie for a PhD fellowship to N.S. We also thank UMICORE for the donation of chemicals. Open Access funding enabled and organized by Projekt DEAL.

Conflict of Interest

The authors declare no conflict of interest.

Keywords: density-functional theory · isomerization · palladium · reaction mechanisms · stereoselectivity

[1] D. Fiorito, S. Scaringi, C. Mazet, *Chem. Soc. Rev.* **2021**, *50*, 1391–1406.
[2] a) D. B. Grotjahn, *Dalton Trans.* **2008**, 6497–6508; b) A. Vasseur, J. Bruffaerts, I. Marek, *Nat. Chem.* **2016**, *8*, 209–219; c) S. Murahashi in *Ruthenium in Organic Synthesis*, Wiley-VCH, Weinheim, **2004**, pp. 309–331; d) D. B. Grotjahn, *Top. Catal.* **2010**, *53*, 1009–1014; e) G. Hilt, *ChemCatChem* **2014**, *6*, 2484–2485; f) W. A. Herrmann, M. Prinz, in *Applied Homogeneous Catalysis with Organometallic Compounds, 2nd ed.* (Eds.: B. Cornils, W. A. Herrmann), Wiley-VCH, Weinheim, Germany, **2002**, p. 1119–1130; g) R. H. Crabtree, *in The Organometallic Chemistry of the Transition Metals, 5th ed.*, John Wiley & Sons, Hoboken, **2009**, pp. 229–231; h) J. C. Mol, *J. Mol. Catal. A* **2004**, *213*, 39–45; i) P. W. N. M. van Leeuwen in *Homogeneous Catalysis: Understanding the Art*, Kluwer Academic, Dordrecht, **2004**, pp. 101–107; j) B. Schmidt, *Eur. J. Org. Chem.* **2004**, 1865–1880; k) S. Otsuka, K. Tani in *Transition Metals for Organic Synthesis, 2nd ed.*, Wiley-VCH, Weinheim, **2004**, pp. 199–209; l) A. Scarso, M. Colladon, P. Sgarbossa, C. Santo, R. A. Michelin, G. Strukul, *Organometallics* **2010**, *29*, 1487–1497; m) C. P. Casey, C. R. Cyr, *J. Am. Chem. Soc.* **1973**, *95*, 2240–2248; n) M. Mayer, A. Welther, A. Jacobi von Wangelin, *ChemCatChem* **2011**, *3*, 1567–1571; o) R. Jennerjahn, R. Jackstell, I. Piras, R. Franke, H. Jiao, M. Bauer, M. Beller, *ChemSusChem* **2012**, *5*, 734–739; p) L.-G. Zhuo, Z.-K. Yao, Z.-X. Yu, *Org. Lett.* **2013**, *15*, 4634–4637; q) C. Chen, T. R. Dugan, W. W. Brennessel, D. J. Weix, P. L. Holland, *J. Am. Chem. Soc.* **2014**, *136*, 945–955; r) G. Erdogan, D. B. Grotjahn, *Org. Lett.* **2014**, *16*, 2818–2821; s) C. R. Larsen, G. Erdogan, D. B. Grotjahn, *J. Am. Chem. Soc.* **2014**, *136*, 1226–1229; t) S. M. M. Knapp, S. E. Shaner, D. Kim, D. Y. Shopov, J. A. Tendler, D. M. Pudalov, A. R. Chianese, *Organometallics* **2014**, *33*, 473–484.
[3] a) M. P. Doyle, G. A. Devora, A. O. Nefedov, K. G. High, *Organometallics* **1992**, *11*, 549–555; b) W.-C. Lee, C.-H. Wang, Y.-H. Lin, W.-C. Shih, T.-G. Ong, *Org. Lett.* **2013**, *15*, 5358–5361; c) T. J. Donohoe, T. J. C. O'Riordan, C. P. Rosa, *Angew. Chem. Int. Ed.* **2009**, *48*, 1014–1017; *Angew. Chem.* **2009**, *121*, 1032–1035.
[4] G. W. Parshall, S. D. Ittel in *Homogeneous Catalysis, 2nd ed.*, Wiley-VCH, Weinheim, **1992**, p. 9.
[5] a) A. Seayad, M. Ahmed, H. Klein, R. Jackstell, T. Gross, M. Beller, *Science* **2002**, *297*, 1676–1678; b) P. W. N. M. van Leeuwen, *Homogeneous Catalysis: Understanding the Art*, Springer, **2004**; c) A. S. Goldman, A. H. Roy, Z. Huang, R. Ahuja, W. Schinski, M. Brookhart, *Science* **2006**, *312*, 257–261; d) S. Biswas, Z. Huang, Y. Choliy, D. Y. Wang, M. Brookhart, K.

 © 2021 The Authors. Chemistry - A European Journal published by Wiley-VCH GmbH

Krogh-Jespersen, A. S. Goldman, *J. Am. Chem. Soc.* **2012**, *134*, 13276–13295.
[6] A. Cybulski, *Fine Chemicals Manufacture: Technology and Engineering*; Elsevier, Amsterdam, **2001**.
[7] "Production of 2-methyl-2-hepten-6-one[P]", H. Müller, H. Koehl, H. Pommer (BASF, USA), US 3.670.028, **1972**.
[8] a) W. C. Seidel, C. A. Tolman, *Annal. N. Y. Acad. Sci.* **1983**, *415*, 201–221; b) A. Behr, D. Obst, A. Westfechtel, *Eur. J. Lipid Sci. Technol.* **2005**, *107*, 213–219; c) C. Jiménez-Rodriguez, G. R. Eastham, D. J. Cole-Hamilton, *Chem. Commun.* **2004**,1720–1721; d) C. Jiménez-Rodriguez, G. R. Eastham, D. J. Cole-Hamilton, *Inorg. Chem. Commun.* **2005**,*8*, 878–881; e) D. Quinzler, S. Mecking, *Angew. Chem. Int. Ed.* **2010**, *49*, 4306–4308; *Angew. Chem.* **2010**, *122*, 4402–4404.
[9] D. E. Fogg, E. N. dos Santos, *Coord. Chem. Rev.* **2004**, *248*, 2365–2379.
[10] a) M. B. France, J. Feldman, R. H. Grubbs, *J. Chem. Soc. Chem. Commun.* **1994**, 1307–1308; b) C. S. Consorti, G. L. P. Aydos, J. Dupont, *Chem. Commun.* **2010**, *46*, 9058–9060.
[11] a) V. Durà-Vilà, D. M. P. Mingos, R. Vilar, A. J. P. White, D. J. Williams, *J. Organomet. Chem.* **2000**, *600*, 198–205; b) V. Durà-Vilà, D. M. P. Mingos, R. Vilar, A. J. P. White, D. J. Williams, *Chem. Commun.* **2000**, 1525–1526; c) M. Prashad, X. Y. Mak, Y. Liu, O. Repic, *J. Org. Chem.* **2003**, *68*, 1163–1164; d) J. P. Stambuli, R. Kuwano, J. F. Hartwig, *Angew. Chem. Int. Ed.* **2002**, *41*, 4746–4748; *Angew. Chem.* **2002**, *114*, 4940–4942.
[12] P. Mamone, M. F. Grünberg, A. Fromm, B. A. Khan, L. J. Gooßen, *Org. Lett.* **2012**, *14*, 3716–3719.
[13] L. Porri, P. Diversi, A. Lucherini, R. Rossi, *Makromol. Chem.* **1975**, *176*, 3121–3125.
[14] M. B. France, J. Feldman, R. H. Grubbs, *J. Chem. Soc. Chem. Commun.* **1994**, 1307–1308.
[15] a) A. S. Carlsson, J. L. Yilmaz, A. G. Green, S. Stymne, P. Hofvander, *Eur. J. Lipid Sci. Technol.* **2011**, *113*, 812–831; b) K. Hill, *Pure Appl. Chem.* **2007**, *79*, 1999–2011; c) J. C. Ronda, G. Lligadas, M. Galià, V. Cádiz, *Eur. J. Lipid Sci. Technol.* **2011**, *113*, 46–58; d) M. A. R. Meier, J. O. Metzger, U. S. Schubert, *Chem. Soc. Rev.* **2007**, *36*, 1788–1802; e) Y. Xia, R. C. Larock, *Green Chem.* **2010**, *12*, 1893–1909.
[16] D. M. Ohlmann, N. Tschauder, J.-P. Stockis, K. Gooßen, M. Dierker, L. J. Gooßen, *J. Am. Chem. Soc.* **2012**, *134*, 13716–13729.
[17] S. Baader, D. M. Ohlmann, L. J. Gooßen, *Chem. Eur. J.* **2013**, *19*, 9807–9810.
[18] S. Baader, P. E. Podsiadly, D. J. Cole-Hamilton, L. J. Gooßen, *Green Chem.* **2014**, *16*, 4885–4890.
[19] A. S. Trita, L. C. Over, J. Pollini, S. Baader, S. Riegsinger, M. A. R. Meier, L. J. Gooßen, *Green Chem.* **2017**, *19*, 3051–3060.
[20] K. F. Pfister, S. Baader, M. Baader, S. Berndt, L. J. Gooßen, *Sci. Adv.* **2017**, *3*, No. e1602624.
[21] A. J. Hubert, H. Reimlinger, *Synthesis* **1970**, *8*, 405–430.
[22] A. J. Hubert, H. Reimlinger, *Synthesis* **1969**, *3*, 97–112.
[23] Y. Ichinose, K. Nozaki, K. Wakamatsu, K. Oshima, K. Utimoto, *Tetrahedron Lett.* **1987**, *28*, 3709–3712.
[24] a) A. R. Daniewski, L. M. Garofalo, S. D. Hutchings, M. M. Kabat, W. Liu, M. Okabe, R. Radinov, G. P. Ylannikouros, *J. Org. Chem.* **2002**, *67*, 1580–1587; b) A. V. Smarun, W. Shahreel, S. Pramono, S. Y. Koo, L. Y. Tan, R. Ganguly, D. Vidović, *J. Organomet. Chem.* **2017**, *834*, 1–9.
[25] S. De, N. Sivendran, B. Maity, N. Pirkl, D. Koley, L. J. Gooßen, *ACS Catal.* **2020**, *10*, 4517–4533.
[26] E. Larionov, L. Lin, L. Guénée, C. Mazet, *J. Am. Chem. Soc.* **2014**, *136*, 16882–16894.
[27] M. J. Frisch, et al., *Gaussian 09, Rev. D.01*, Gaussian, Inc., Wallingford, CT, **2013**.
[28] a) A. D. Becke, *J. Chem. Phys.* **1993**, *98*, 5648–5652; b) C. Lee, W. Yang, R. G. Parr, *Phys. Rev. B: Condens. Matter Mater. Phys.* **1988**, *37*, 785–789.
[29] a) S. Grimme, J. Antony, S. Ehrlich, H. Krieg, *J. Chem. Phys.* **2010**, *132*, 154104–154122; b) A. D. Becke, *Phys. Rev. A* **1988**, *38*, 3098–3100.
[30] W. J. Hehre, L. Radom, L. v. R. Schleyer, J. A. Pople, *Ab Initio Molecular Orbital Theory*, Wiley, New York, NY, **1986**.
[31] a) P. J. Hay, W. R. Wadt, *J. Chem. Phys.* **1985**, *82*, 270–283; b) W. R. Wadt, P. J. Hay, *J. Chem. Phys.* **1985**, *82*, 284–298; c) P. J. Hay, W. R. Wadt, *J. Chem. Phys.* **1985**, *82*, 299–310.
[32] T. A. Halgren, W. N. Lipscomb, *Chem. Phys. Lett.* **1977**, *49*, 225–232.
[33] a) H. P. Hratchian, H. B. Schlegel in *Theory and Applications of Computational Chemistry: The First 40 Years* (Eds: C. E. Dykstra, G. Frenking, K. S. Kim, G. Scuseria), Elsevier, Amsterdam, **2005**, pp. 195–249; b) H. P. Hratchian, H. B. Schlegel, *J. Chem. Theory Comput.* **2005**, *1*, 61–69; c) H. P. Hratchian, H. B. Schlegel, *J. Chem. Phys.* **2004**, *120*, 9918–9924; d) K. Fukui, *Acc. Chem. Res.* **1981**, *14*, 363–368.
[34] A. V. Marenich, C. J. Cramer, D. G. Truhlar, *J. Phys. Chem. B.* **2009**, *113*, 6378–6396.
[35] a) S. Khan, R. Michel, D. Koley, H. W. Roesky, D. Stalke, *Inorg. Chem.* **2011**, *50*, 10878–10883; b) S. Khan, R. Michel, S. S. Sen, H. W. Roesky, D. Stalke, *Angew. Chem. Int. Ed.* **2011**, *50*, 11786–11789; *Angew. Chem.* **2011**, *123*, 11990–11993.
[36] a) J. Cooper, T. Ziegler, *Inorg. Chem.* **2002**, *41*, 6614–6622; b) S. Tobisch, *Chem. Eur. J.* **2005**, *11*, 3113–3126; c) S. Di Tommaso, V. Tognetti, E. Sicilla, C. Adamo, N. Russo, *Inorg. Chem.* **2010**, *49*, 9875–9883; d) B. Maity, L. J. Gooßen, D. Koley, *Chem. Sci.* **2015**, *6*, 2532–2552.
[37] a) E. R. Johnson, S. Keinan, P. Mori-Sanchez, J. Contreras-García, A. J. Cohen, W. Yang, *J. Am. Chem. Soc.* **2010**, *132*, 6498−6506; b) J. Contreras-García, E. R. Johnson, S. Keinan, R. Chaudret, J.-P. Piquemal, D. N. Beratan, W. Yang, *J. Chem. Theory Comput.* **2011**, *7*, 625−632.
[38] K. J. Morokuma, *Chem. Phys.* **1971**, *55*, 1236–1244.
[39] a) T. Ziegler, A. Rauk, *Inorg. Chem.* **1979**, *18*, 1755–1759; b) T. Ziegler, A. Rauk, *Inorg. Chem.* **1979**, *18*, 1558–1565.
[40] G. teVelde, F. M. Bickelhaupt, E. J. Baerends, C. Fonseca Guerra, S. J. A. Van Gisbergen, J. G. Snijders, T. Ziegler, *J. Comput. Chem.* **2001**, *22*, 931–967.
[41] a) A. D. Becke, *Phys. Rev. A* **1988**, *38*, 3098–3100; b) J. P. Perdew, *Phys. Rev. B: Condens. Matter Mater. Phys.* **1986**, *33*, 8822–8824; c) S. Grimme, J. Antony, S. Ehrlich, H. Krieg, *J. Chem. Phys.* **2010**, *132*, 154104.
[42] a) E. V. Lenthe, E. J. Baerends, *J. Comput. Chem.* **2003**, *24*, 1142–1156; b) D. P. Chong, E. V. Lenthe, S. V. Gisbergen, E. J. Baerends, *J. Comput. Chem.* **2004**, *25*, 1030–1036.
[43] E. Lenthe, E. J. Baerends, J. G. Snijders, *J. Chem. Phys.* **1994**, *101*, 9783–9792.
[44] a) G. Frenking, K. Wichmann, N. Fröhlich, C. Loschen, M. Lein, J. Frunzke, V. M. Rayón, *Coord. Chem. Rev.* **2003**, *238–239*, 55–82; b) A. Krapp, F. M. Bickelhaupt, G. Frenking, *Chem. Eur. J.* **2006**, *12*, 9196–921.
[45] C. Y. Legault, *CYLView, 1.0b*, Université de Sherbrooke: Sherbrooke (Canada), **2009**, http://www.cylview.org.
[46] E. M. Simmons, J. F. Hartwig, *Angew. Chem. Int. Ed.* **2012**, *51*, 3066–3072; *Angew. Chem.* **2012**, *124*, 3120–3126.
[47] M. Besora, F. Maseras, *WIREs Comput. Mol. Sci.* **2018**, *8*, e1372.
[48] a) A. Otero-de-la-Roza, E. R. Johnson, J. Contreras-García, *Phys. Chem. Chem. Phys.* **2012**, *14*, 12165–12172; b) R. Laplaza, F. Peccati, R. A. Boto, C. Quan, A. Carbone, J.-P. Piquemal, Y. Maday, J. Contreras-García, *WIREs Comput. Mol. Sci.* **2021**, *11*, e1497.
[49] a) M. Pareek, R. B. Sunoj, *ACS Catal.* **2016**, *6*, 3118–3126; b) B. W. Bakra, C. D. Sherrill, *Phys. Chem. Chem. Phys.* **2016**, *18*, 10297–10308; c) H. Sabet-Sarvestani, H. Eshghi, M. Izadyar, M. Bakavoli, *J. Inclusion Phenom. Macrocyclic Chem.* **2016**, *85*, 237–246.
[50] a) S. Dutta, S. De, S. Bose, E. Mahal, D. Koley, *Eur. J. Inorg. Chem.* **2020**, *2020*, 638–655; b) T. Mondal, S. Dutta, S. De, D. Koley, *J. Org. Chem.* **2019**, *84*, 257–272; c) S. Dutta, T. Mondal, S. De, K. Rudra, D. Koley, *Inorg. Chim. Acta* **2019**, *485*, 162–172; d) S. Dutta, B. Maity, D. Thirumalai, D. Koley, *Inorg. Chem.* **2018**, *57*, 3993–4008; e) T. Mondal, S. De, D. Koley, *Inorg. Chem.* **2017**, *56*, 10633–10643.

Manuscript received: July 14, 2021
Accepted manuscript online: August 13, 2021
Version of record online: September 20, 2021

 © 2021 The Authors. Chemistry - A European Journal published by Wiley-VCH GmbH